

Searching for axionlike particles from core-collapse supernovae with *Fermi* LAT's low-energy technique

Milena Crnogorčević^{*}

*Department of Astronomy, University of Maryland, College Park, Maryland 20742, USA
and Center for Research and Exploration in Space Science and Technology,
NASA Goddard Space Flight Center, Greenbelt, Maryland 20771, USA*

Regina Caputo

NASA Goddard Space Flight Center, Greenbelt, Maryland 20771, USA

Manuel Meyer

*Institute for Experimental Physics, University of Hamburg,
Luruper Chaussee 149, 22671 Hamburg, Germany*

Nicola Omodei

*W. W. Hansen Experimental Physics Laboratory, Kavli Institute for Particle Astrophysics and Cosmology,
Department of Physics and SLAC National Accelerator Laboratory, Stanford University,
Stanford, California 94305, USA*

Michael Gustafsson

*The Oskar Klein Centre for Cosmoparticle Physics, Department of Physics, Stockholm University,
AlbaNova, SE-106 91 Stockholm, Sweden*



(Received 21 May 2021; accepted 9 September 2021; published 1 November 2021)

Light axionlike particles (ALPs) are expected to be abundantly produced in core-collapse supernovae (CCSNe), resulting in a ~ 10 -second long burst of ALPs. These particles subsequently undergo conversion into gamma rays in external magnetic fields to produce a long gamma-ray burst (GRB) with a characteristic spectrum peaking in the 30–100-MeV energy range. At the same time, CCSNe are invoked as progenitors of *ordinary* long GRBs, rendering it relevant to conduct a comprehensive search for ALP spectral signatures using the observations of long GRBs with the *Fermi* Large Area Telescope (LAT). We perform a data-driven sensitivity analysis to determine CCSN distances for which a detection of an ALP signal is possible with the LAT's low-energy technique which, in contrast to the standard LAT analysis, allows for a larger effective area for energies down to 30 MeV. Assuming an ALP mass $m_a \lesssim 10^{-10}$ eV and ALP-photon coupling $g_{a\gamma} = 5.3 \times 10^{-12} \text{ GeV}^{-1}$, values considered and deduced in ALP searches from SN1987A, we find that the distance limit ranges from ~ 0.5 to ~ 10 Mpc, depending on the sky location and the CCSN progenitor mass. Furthermore, we select a candidate sample of 24 GRBs and carry out a model comparison analysis in which we consider different GRB spectral models with and without an ALP signal component. We find that the inclusion of an ALP contribution does not result in any statistically significant improvement of the fits to the data. We discuss the statistical method used in our analysis and the underlying physical assumptions, the feasibility of setting upper limits on the ALP-photon coupling, and give an outlook on future telescopes in the context of ALP searches.

DOI: [10.1103/PhysRevD.104.103001](https://doi.org/10.1103/PhysRevD.104.103001)

I. INTRODUCTION

The axionlike particle (ALP), a generalized case of the QCD axion, belongs to the family of very weakly interacting subelectronvolt particles (WISPs) (see e.g., Refs. [1–4] and references therein for a review of the QCD axion [5–8]).

The interaction of ALPs with photons can be described by the following Lagrangian:

$$\mathcal{L}_{a\gamma} \supset -\frac{1}{4}g_{a\gamma}\mathbf{E}\cdot\mathbf{B}a, \quad (1)$$

where $g_{a\gamma}$ is the photon-ALP coupling, \mathbf{E} is the electric field, \mathbf{B} is the magnetic field, and a represents the ALP

^{*}mcrnogor@astro.umd.edu

field. When an external magnetic field \mathbf{B} is present, the two-photon coupling results in a photon-ALP conversion [9]. Photon-ALP oscillations have been invoked to explain the excess of soft x rays from the center of galaxy clusters [10–13], the monochromatic 3.55-keV line in galaxy clusters [14], the low opacity of the Universe to TeV photons [15–19], anomalous stellar cooling [20–23], as well as the low-energy electronic recoil event excess in XENON1T [24–26]. Furthermore, ALPs are considered one of the leading candidates for cold dark matter [27–31]. The ALP parameter space has been explored using various experimental approaches, including light-shining-through-the-wall experiments [32], cavity experiments [33], as well as observations of different astrophysical targets, such as Cepheid variable stars [34], star clusters [35,36], and galaxy clusters [37–41].

In this paper, we investigate the prospect to detect ALPs that are produced in high-energy environments—in particular, core-collapse supernovae (CCSNe)—via the Primakoff resonant process [42], and subsequently travel undisturbed until they reach the Galactic magnetic field where they convert into γ -ray photons [43,44]. For a ten-solar-mass (hereafter denoted by M_\odot) CCSN progenitor, the ALP spectrum should have a thermal shape peaking at around 70 MeV [45–47]. The duration of an ALP-induced burst varies depending on the mass of a progenitor; nevertheless, the signal would be short (on the order of tens of seconds). No other physical processes are predicted to produce such spectral signatures in a CCSN’s γ -ray spectrum. Thus, using observations of a CCSN and, in particular, searching for its presumed associated ALP-induced gamma-ray burst (GRB), can be an excellent probe for constraining the ALP parameter space (e.g. [48,49]).

Ordinary GRBs, believed to arise from collimated ultra-relativistic outflows of materials when, e.g., a star collapses, are among the most luminous events in the Universe, spectrally peaking in the keV–MeV energy range [50]. Depending on the duration of their prompt emission and their spectral hardness, GRBs are divided into two subtypes: the short-hard, for which the emission duration is less than 2 seconds, and long-soft, with their duration exceeding 2 seconds [51,52]. To explain differences between the two subtypes with respect to their duration, flux, variability, spectral parameters and evolution, the nature of their progenitors is often invoked [53]. Short-hard GRBs are suspected to originate from compact-object binary mergers (such as two neutron stars or a neutron star and a black hole [54–56]) and long-soft GRBs are likely associated with type Ib/c CCSNe [57–62]. Taking into account the predicted duration of an ALP-induced burst (a few tens of seconds), as well as the nature of the hypothesized ALP production site (CCSNe), we are particularly interested in studying the long-soft GRBs.

Using the properties of the ALP spectral emission, we first conduct a sensitivity analysis to determine the limiting

distance to which *Fermi* Gamma-ray Observatory [63,64] would be able to detect an ALP-induced GRB using the LAT low-energy technique [65]. Considering astrophysical background levels from GRBs observed at various incidence angles, we estimate the necessary ALP flux that would lead to a significant detection of the ALP induced gamma-ray burst. Second, we consider a selected GRB sample and conduct a model comparison between fits that include the ALP spectral component and those that do not. Finally, we discuss the found limiting distances, the feasibility of upper limits on ALP couplings, and the tangibility of ALP detection with *Fermi* or other gamma-ray observatories alike.

This paper is organized as follows: Section II provides an overview of the ALP spectral model, derived in [47]. In Sec. III, we describe the GRB data selection process. In Sec. IV, we conduct a sensitivity study to determine the CCSN distances and photon-ALP couplings that would result in a significant detection of a GRB in the relevant MeV energy range with *Fermi*. Section V describes the ALP-fitting method for the selected sample of GRBs. Finally, Sec. VI provides the summary and future outlooks for ALP searches within the gamma-ray energy band.

II. ALP MODEL

To produce a spectral model for an ALP-induced GRB as observed on Earth, we utilize the one-dimensional CCSN (ALP-induced GRB) model derived in [47] that is, due to the complexity of core-collapse modeling, available for only two distinct progenitor masses (10 M_\odot and 18 M_\odot). The temporal and energy evolution of an ALP burst emission are shown in Fig. 1.

The observed photon flux, $d\phi_\gamma/dE$, can be expressed as

$$\frac{d\phi_\gamma}{dE} = \frac{P_{a\gamma}(g_{a\gamma})}{4\pi d^2} \frac{d\dot{N}_a(g_{a\gamma})}{dE}, \quad (2)$$

where d is the luminosity distance to the CCSN; $P_{a\gamma}$ is the ALP-photon conversion probability, proportional to $g_{a\gamma}^2$; and \dot{N}_a/dE is the Primakoff production rate of ALPs per unit energy, also proportional to $g_{a\gamma}^2$. This proportionality, $P_{a\gamma} \propto g_{a\gamma}^2$, breaks down before $P_{a\gamma}$ approaches unity [66]. The total flux normalization may then be written as

$$N_{\text{tot}} = 8.4 \times 10^{-54} \text{ cm}^{-2} \left(\frac{d}{10 \text{ Mpc}} \right)^{-2} \times \left(\frac{g_{a\gamma}}{g_0} \right)^4 \times \left(\frac{P_{a\gamma}(g_0)}{0.1} \right), \quad (3)$$

with $g_0 = 10^{-11} \text{ GeV}^{-1}$ denoting an arbitrary reference coupling, roughly corresponding to the current upper limit, $g_{a\gamma} \lesssim 5.3 \times 10^{-12} \text{ GeV}^{-1}$ [47], for ALP masses ranging from $m_a \simeq 10^{-12}$ to 10^{-8} eV [37,38,40,47,67].

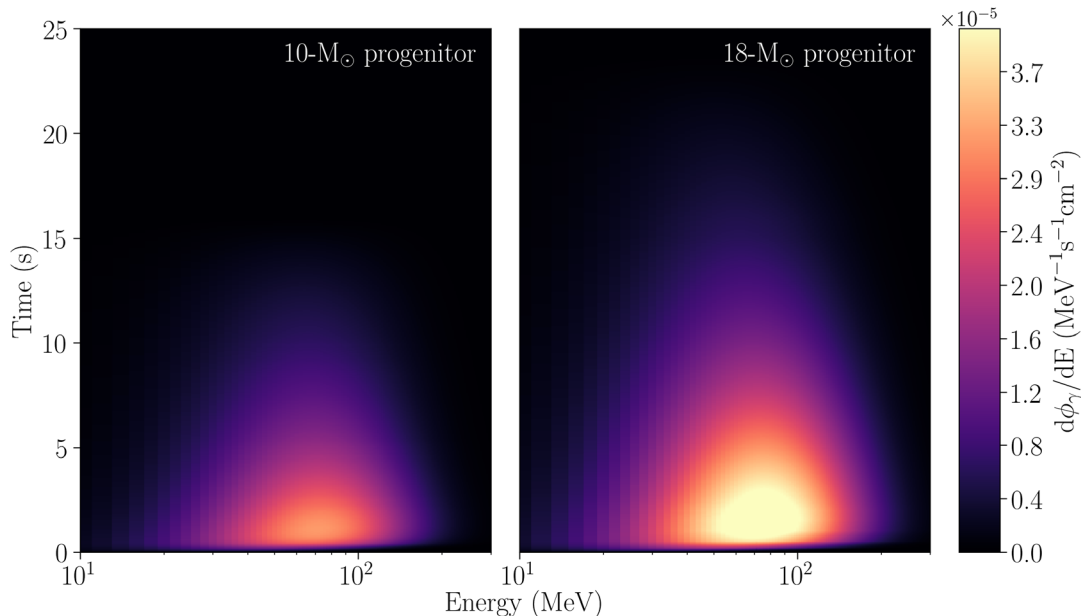


FIG. 1. Observed evolution of the ALP-induced gamma-ray emission in time and energy in a core collapse of a 10- and 18- M_{\odot} progenitor, normalized by $N_{\text{tot}} = 8.4 \times 10^{-54} \text{ cm}^{-2}$. Note that most of the emission occurs in the first ten seconds after the collapse. The 18- M_{\odot} progenitor is a more energetic source of ALPs with a few-second prolonged emission as compared to the 10- M_{\odot} progenitor.

For lower-mass ALPs, i.e., $m_a \lesssim 10^{-12} \text{ eV}$, observations of galaxy clusters provide more stringent constraints, $g_{a\gamma} \lesssim 6\text{--}8 \times 10^{-13} \text{ GeV}^{-1}$ [41] (see also [36,68,69]). Furthermore, for masses $m_a \gtrsim 10^{-10} \text{ eV}$, the conversion probability $P_{a\gamma}$ becomes energy dependent and effectively drops within the MeV energy range considered in this analysis. The observed photon flux can now conveniently be expressed as

$$\frac{d\phi_{\gamma}}{dE} = N_{\text{tot}} \times \frac{\dot{N}_a(g_0)}{dE}. \quad (4)$$

Using the CCSN model in [47], we obtain the temporal and energy information about the ALP production rates $d\dot{N}_a(g_0)/dE$ in a core collapse due to the ALP interactions described in Eq. (1). Figure 1 shows that most of the corresponding ALP-induced gamma-ray emission happens in the first few tens of seconds for both progenitor masses; hence, by averaging over the time interval of 10 seconds starting at the core collapse, we obtain the expected spectra shown in Fig. 2.

A. Conversion probability

The photon-ALP conversion probability, $P_{a\gamma}$, is computed numerically to account for variations in the Galactic magnetic field. Following the Milky Way magnetic field model by Jansson and Farrar [70], we compute the conversion probabilities for different positions in the sky, assuming that the photon-ALP mixing happens throughout the entire Galaxy, as done in [48,71]. The contribution from the turbulent magnetic field component is not included in this analysis since its typical coherence length ($\sim 10 \text{ pc}$) is

significantly shorter than the ALP-photon oscillation length and can be neglected for the considered ALP mass $m_a \lesssim 10^{-10} \text{ eV}$ in most sky regions [72,73]. For an emission that passes only through the Galactic magnetic field, the conversion probability is shown in Fig. 3, as a function of the source's position in the sky. We assume that $P_{a\gamma}$ is energy independent in our analysis, which is valid for low-mass ALPs ($m_a \lesssim 10^{-10} \text{ eV}$), while for larger ALP masses $P_{a\gamma} = P_{a\gamma}(g_{a\gamma}, m_a, E)$ decreases and starts to oscillate as a function of energy [47].

We do not take into account the photon-ALP conversions that may happen in the intergalactic magnetic field, as such

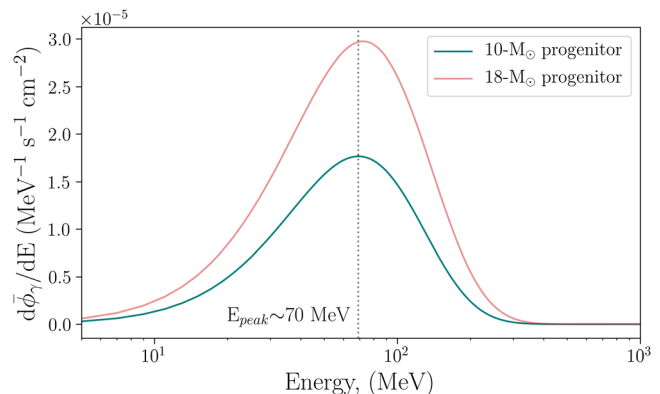


FIG. 2. The observed ALP-induced gamma-ray spectrum for 10- and 18- M_{\odot} progenitors integrated and averaged over the first 10 seconds after the collapse for a normalization, $N_{\text{tot}} = 8.4 \times 10^{-54} \text{ cm}^{-2}$ [see Eq. (3)]. Note that most of the flux is emitted around 70 MeV.

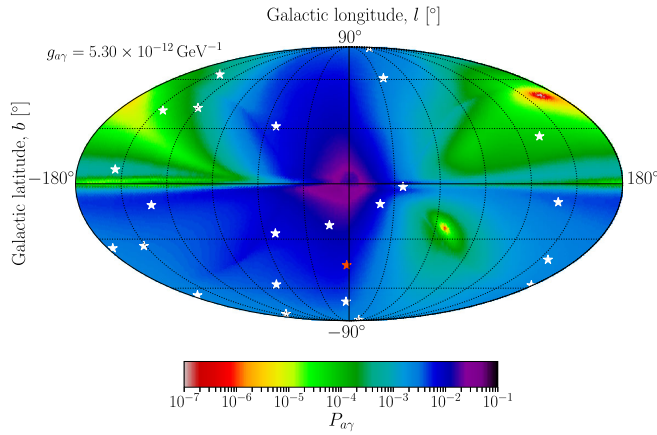


FIG. 3. ALP-photon conversion probability as a function of source position in the sky. We consider only the ALP conversion into gamma rays within the Milky Way’s coherent magnetic field component, as modeled in [48]. We assume an ALP mass $m_a = 10^{-10}$ eV and coupling $g_{a\gamma} = 5.3 \times 10^{-12}$ GeV $^{-1}$, and energy $10 < E < 300$ MeV. Note that for this configuration, $P_{a\gamma, \max} \sim 0.1$ is the maximum conversion probability reached in the central regions of the Milky Way. White crosses represent the best localization positions of the GRB sample considered in Sec. V, with the red cross corresponding to GRB 101123A [74].

contributions would be negligible and highly uncertain for the nearby sources we consider. For example, if we assume a uniform intergalactic magnetic field strength of ~ 1 nG, a coupling of $g_{a\gamma} = 5.3 \times 10^{-12}$ GeV $^{-1}$ and a distance of 5 Mpc, we obtain that in the strong-mixing regime (here reached for $m_a \lesssim 10^{-11}$ eV) [15], the order of the conversion probability, $\mathcal{O}(P_{a\gamma})$, is 10^{-3} . Furthermore, considering the conversion probability in an extragalactic source’s host galaxy and, if applicable, its surrounding intracluster medium, would be highly uncertain due to a lack of knowledge of their respective magnetic fields and would have to be taken on a case by case basis. In addition, such consideration would result in an increase of the observed gamma-ray flux [48], resulting in adjustments to Fig. 3 with conversion probabilities unlikely reaching values below 10^{-3} ; hence, neglecting them renders our results conservative. Due to case by case differences, we do not take into consideration the ALP-photon conversion that may take place in the magnetic field of the intergalactic medium and within the host galaxy.

B. ALP model in XSPEC

Spectral modeling in this paper is conducted using the standard high-energy fitting package XSPEC [75] and its Python adaptation, PYXSPEC [76]. The ALP spectra shown in Fig. 2 are used to write a model function that is inserted into the XSPEC model library using the `addPyMod` method. For the model parameters, we consider two different progenitor masses, $10 M_\odot$ and $18 M_\odot$, with the normalization parameter N_{tot} , from Eq. (4), left free to vary.

III. DATA SELECTION

A. Fermi observatory

The *Fermi* observatory provides a wide spectral coverage and excellent sensitivity for studying GRBs. The observatory contains two instruments on board, the Gamma-ray Burst Monitor (GBM, [63]) and the Large Area Telescope (LAT, [64]). The GBM has twelve sodium-iodide (NaI) and two bismuth-germanate (BGO) scintillation detectors, covering 8 keV to 1 MeV and 150 keV to 40 MeV in energy, respectively. The field of view (FoV) is ~ 9.5 sr and the point-source localization accuracy is $\sim 5^\circ$. On the other hand, LAT is a pair production telescope covering the energy range from 20 MeV to more than 300 GeV, with a FoV of ~ 2.4 sr, and a point-source localization of $< 1^\circ$, for energies above 1 GeV. Figure 3 shows the best localization values for the considered GRB sample using either GBM or LAT instruments [74]. Particularly of interest in this paper is the LAT low-energy data (LLE, [65]), due to the energy of the ALP spectral peak at 70 MeV, shown in Fig. 2.

The LLE analysis method was developed with the goal of maximizing the effective area of the LAT instrument in the low-energy regime [65]. This is done by relaxing the requirements on background rejection, as compared to the standard LAT transient analysis. This technique is particularly useful for a study of transients, such as GRBs, for energies greater than ~ 30 MeV. The LLE event selection relies upon having at least one reconstructed track within the LAT’s tracker/converter, allowing for an estimate of the direction of the incoming photon. Furthermore, all photons pass through the anticoincidence detector which enables cosmic-ray background rejection. Finally, this algorithm requires a nonzero reconstructed energy of the considered event. Then, for the short and bright transient sources, the background is determined by an “ON” and “OFF” time-interval technique. The background rate during the “OFF” interval is fit by a polynomial function in each energy bin, providing us with an estimate of the background during the “ON” interval. The corresponding LLE response files are produced using Monte Carlo simulations of bright point sources with a specific spectral shape at the sky position of interest. The systematic effects in reconstructing the LLE events are considered in [77], estimating the discrepancy between the LLE selection criteria in the LAT data and in Monte Carlo simulations to be $\sim 17\%$ for events below 100 MeV. Comparing the flux values reveals that LLE’s flux estimations are on average lower than those from the standard LAT analysis; however, no significant biases are reported for the energy resolution, with that of LLE estimated to $\sim 40\%$ at 30 MeV and $\sim 30\%$ at 100 MeV. A detailed description of the LLE technique is provided in [77]. The LLE data is publicly available from the HEASARC website [78]. In Sec. IV, we focus on utilizing the LLE data sample which, in Sec. V, is complemented by the GBM and the standard LAT transient data, when such observations are available.

B. Time tagging of a core collapse

One of the main challenges for conducting ALP spectral fitting is to observationally approximate the collapse time of a supernova, i.e., the time when most of the ALPs escape the collapse site.

The optimal way to address this challenge is through neutrino detection from the source, as neutrinos and ALPs are expected to arrive at approximately the same time. However, observational neutrino data from supernovae are scarce (so far, only SN1987A [47]). Although the second generation of neutrino detectors has significantly improved in sensitivity (e.g. IceCube detection from the blazar TXS 0506 + 056 at $z = 0.33$ [79]), no neutrino signal detection is expected from an extragalactic supernova in the near future [80]. This imposes tight limitations on a potential ALP-source distance from which a neutrino signal can be detected, likely to a CCSN in our own Galaxy or in the local group, extending up to a few Mpc [80,81]. Furthermore, if we were to use neutrinos for time tagging of a core collapse, we would also require a gamma-ray observation of such an event in order to conduct the ALP spectral fitting. For example, the probability for a Galactic SN to occur in the LAT FoV in the next 3 years is $\lesssim 1\%$.

Beside neutrino detection, another way to approximate explosion times of supernovae is by using their optical light curves [82]. This technique has been used in [49] to search for an ALP-induced gamma-ray burst with the standard LAT data above 60 MeV.

Another possibility to infer the core-collapse time is from the time of the ordinary astrophysical GRB. The ordinary bursts are delayed on the order of seconds to minutes with respect to the core collapse, as the jet needs to form and propagate through the stellar envelope (see, e.g., Fig. 10.1 in [83]). Moreover, the ALP-induced gamma-ray emission is approximately isotropic from the source, in contrast to the ordinary GRB jet emission—which also might not be aligned with our line of sight, resulting in a considerably weaker signal if seen off axis (or even a “failed GRB” [84]). This could imply that not every ALP signal is accompanied by a subsequent ordinary GRB detection. A dedicated study regarding precursor emission (hypothetically, an ALP signal prior to the observed jet emission) to GRBs may address the time-tagging issue in more detail and is a matter for future research. In this paper, we assume that the time when most ALPs escape the collapse site coincides with the GRB signal time window.

C. GRB selection criteria

Considering the GRBs detected so far by *Fermi*-LAT [74], with their corresponding optical follow-ups and, in turn, redshift information, we infer that all associated sources are too far (the closest one being over 600 Mpc away) to be considered for a sizable ALP-induced burst observation (see the sensitivity results of Sec. IV C). Thus, in our analysis we instead only consider all the

LLE-detected GRBs without redshift information (hereafter referred to as *unassociated* GRBs) as potential ALP signal candidates; albeit, most likely ordinary GRBs of extragalactic origin. With limited information on the origin of the considered GRB sample, we assume they are either induced by an ALP signal or by ordinary astrophysical processes traditionally applied in GRB spectral modeling (see, e.g., [74]). This allows us to start the ALP analysis at the GRB trigger time, T_0 , with the considered time window encompassing either (or both) the traditional GRB emission and the potential ALP signal.

We consider all unassociated GRB detections by *Fermi* LAT from August 2008 to August 2018, as reported in the *Fermi* LAT Second Gamma-Ray Burst Catalog, 2FLGC [74], publicly available on the HEASARC website [85]. Motivated by the energy of the ALP spectral peak at ~ 70 MeV, we further restrict our sample to GRBs with at least 5σ detection in LLE alone. Such a strong signal in the low-sensitivity region of LAT often indicates a strong signal in either GBM, or standard LAT (or both), often meriting follow-up observations by optical telescopes. Thus, the 5σ requirement combined with no redshift information are the most exclusive cut criteria for our sample. We require the source to be within the FoV throughout the entire duration of the burst which, required by the nature of ALP emission, should be a long GRB. For the sensitivity analysis (Sec. IV), in order to somewhat increase our GRB background sample, we drop the GRB duration criterion as we are only concerned with the observed background levels, which are independent from the GRB’s duration. This results in three additional short GRBs (GRB 081024B, GRB 090227B, and GRB 110529A) which can be used as background templates. As such, the spatial distribution of all the considered GRBs, as shown in Fig. 3, forms a representative sample of the GRB sources in the sky.

The GRB selection criteria are summarized in Table I. From the initial sample of 186 LAT-detected GRBs,

TABLE I. Selection criteria applied to GRBs detected by *Fermi*-LAT between August 2008 to August 2018. From the initial sample size of 186 GRBs, we narrow down the list of candidates to 24 shown in Table II. The burst duration criterion is not applied to the sensitivity analysis in Sec. IV, allowing for the inclusion of three additional short GRBs.

Property	Selection criterion
Distance	Unassociated (no redshift)
Detection significance	$\geq 5\sigma$ in LAT-LLE ($\gtrsim 30$ MeV)
Observed time interval	\geq Duration of the GRB ^a
Burst duration	Long GRBs ($T_{95} \gtrsim 2$ seconds ^b) (<i>not used in Sec. IV</i>)

^aWe select only the GRBs that are within LAT’s FoV throughout their entire duration. Furthermore, we consider a few-hundred-second padding before and after the burst duration for modeling the background emission.

^bAs reported in Table III in [74].

TABLE II. List of the 24 GRBs that pass the selection criteria. T_{95} corresponds to the duration reported in Table III in [74], as seen by GBM. The following columns show the best-fit models listed without an additional ALP component, with uncertainties representing the 90% confidence interval for the given fit parameter. Also included are the log-likelihood ratio (LLR) Λ values, $\Lambda = -2 \log(L_{\text{GRB}}/L_{\text{GRB+ALP}})$, which are derived in Sec. V. We also report the best-fit parameters for the cases in which the Band model (denoted by XSPEC's `grbm`) is one of the model components [86], to demonstrate that the parameters do not reproduce the ALP spectral shape which may be reproduced with $\alpha_1 \sim -2.4$, $\alpha_2 \sim -0.1$, and $E_c \sim 30$ MeV. Details of the GRB analysis are described in Sec. V.

GRB	T_{95} (s)	Best model(no ALP)	grbm parameters			LLR
			α_1	α_2	E_c (keV)	
080825C	22.2	grbm	$-0.65^{+0.05}_{-0.05}$	$-2.41^{+0.04}_{-0.04}$	143^{+13}_{-12}	0.2
090217	34.1	grbm	$-1.11^{+0.04}_{-0.04}$	$-2.43^{+0.03}_{-0.04}$	16^{+13}_{-8}	0.1
100225A	12.7	grbm	$-0.50^{+0.25}_{-0.21}$	$-2.28^{+0.07}_{-0.09}$	223^{+112}_{-68}	0.0
100826A	93.7	grbm+bb	$-1.02^{+0.04}_{-0.04}$	$-2.30^{+0.03}_{-0.04}$	484^{+72}_{-63}	0.0
101123A	145.4	grbm+cutoffpl	$-1.00^{+0.07}_{-0.08}$	$-1.94^{+0.15}_{-0.12}$	187^{+74}_{-62}	5.8
110721A	21.8	grbm+bb	$-1.24^{+0.02}_{-0.01}$	$-2.29^{+0.03}_{-0.03}$	1000^{+28}_{-39}	0.0
120328B	33.5	grbm+cutoffpl	$-0.67^{+0.06}_{-0.05}$	$-2.26^{+0.05}_{-0.05}$	101^{+12}_{-13}	0.0
120911B	69.0	grbm	$-2.50^{+0.92}_{-1.04}$	$-1.05^{+0.63}_{-0.38}$	11^{+10}_{-2}	0.0
121011A	66.8	grbm	$-1.08^{+0.10}_{-0.21}$	$-2.18^{+0.11}_{-0.16}$	997^{+84}_{-26}	0.0
121225B	68.0	grbm	$-2.38^{+1.02}_{-0.40}$	$-2.45^{+0.06}_{-0.07}$	11^{+89}_{-3}	0.0
130305A	26.9	grbm	$-0.76^{+0.03}_{-0.03}$	$-2.63^{+0.06}_{-0.06}$	665^{+61}_{-55}	0.0
131014A	4.2	grbm	$-0.55^{+0.33}_{-0.98}$	$-2.65^{+0.17}_{-0.19}$	255^{+36}_{-11}	0.63
131216A	19.3	grbm+cutoffpl	$-0.46^{+0.28}_{-0.24}$	$-2.67^{+1.94}_{-0.94}$	178^{+77}_{-92}	0.0
140102A	4.1	grbm+bb	$-1.10^{+0.12}_{-0.09}$	$-2.41^{+0.16}_{-0.11}$	206^{+65}_{-92}	2.3
140110A	9.2	grbm	$-2.49^{+1.64}_{-1.59}$	$-2.19^{+0.20}_{-0.22}$	11^{+23}_{-3}	0.0
141207A	22.3	grbm+bb	$-1.21^{+0.09}_{-0.06}$	$-2.33^{+0.11}_{-0.13}$	999^{+18}_{-70}	0.0
141222A	2.8	grbm+pow	$-1.57^{+0.03}_{-0.02}$	$-2.83^{+0.46}_{-1.74}$	9971^{+390}_{-832}	0.0
150210A	31.3	grbm+pow	$-0.52^{+0.04}_{-0.05}$	$-2.91^{+0.11}_{-0.38}$	1000^{+517}_{-234}	0.0
150416A	33.8	grbm	$-1.18^{+0.04}_{-0.04}$	$-2.36^{+0.13}_{-0.21}$	999^{+187}_{-269}	0.0
150820A	5.1	grbm	$-0.99^{+0.56}_{-1.30}$	$-2.01^{+0.82}_{-0.27}$	303^{+61}_{-39}	0.0
151006A	95.0	grbm	$-1.35^{+0.06}_{-0.03}$	$-2.24^{+0.07}_{-0.08}$	998^{+33}_{-84}	0.0
160709A	5.4	grbm+cutoffpl	$-1.44^{+0.18}_{-0.12}$	$-2.18^{+0.15}_{-0.18}$	9940^{+373}_{-511}	1.0
160917A	19.2	grbm+bb	$-0.78^{+3.45}_{-1.40}$	$-2.39^{+0.20}_{-0.10}$	994^{+634}_{-216}	0.9
170115B	44.8	grbm	$-0.80^{+0.02}_{-0.04}$	$-3.00^{+0.10}_{-0.07}$	1000^{+226}_{-106}	2.8

applying the above selection cuts results in a sample of 24 long GRBs, all listed in Table II.

IV. SENSITIVITY ANALYSIS

We conduct a sensitivity study using the LLE data for two reasons: first, to ensure that a manually injected ALP feature can be recognized by our fitting algorithm; second, to determine the maximum distance for a given photon-ALP coupling for which the ALP feature is still significantly detectable in LLE. We also find the distance to a CCSN that allows for setting competitive upper limits on the photon-ALP coupling with *Fermi* LLE. In this study, we use a background energy spectrum derived from three different GRB observations and manually inject the ALP-induced gamma-ray signal that is subsequently folded with the instrument response function.

A. Background considerations

We extract background information for each individual GRB using the analysis tool developed by the LAT team, *gtburst*. This tool allows for a selection of the off-signal intervals, which are fitted in each energy channel with a polynomial function in time, resulting in a fitted background count rate. A detailed description of the GRB analysis process with *gtburst* may be found in Sec. V.

Once we obtain the background count rates, we compute their fluences by conducting spectral fitting using a power-law model, half-Gaussian profile, or a combination thereof to find the lowest, highest, and typical values of background fluences for the LLE data selection, for energies starting at ~ 30 MeV and reaching the GeV energies. In addition to the GRB sample listed in Table II, we include three supplementary short GRBs that pass the remaining

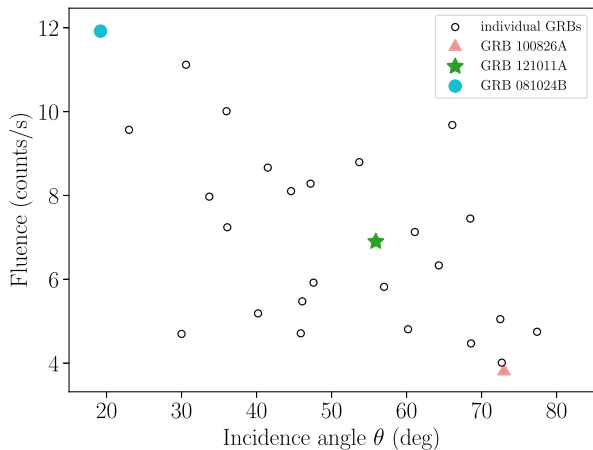


FIG. 4. Background fluences plotted against the incidence angles to the detector, θ . Pink triangle, green star, and blue circle respectively correspond to the lowest, median, and highest background fluences in the sample. Note, however, that low count numbers may be caused by a significant drop in LLE effective area at high θ s.

selection criteria, GRB 081024B, GRB 090227B, and GRB 110529A. The found fluences for GRB backgrounds are computed and plotted as a function of the incidence angle θ , shown in Fig. 4. It is important to note that for large incidence angles, the LLE effective area drops significantly, resulting in low count rates. In our sensitivity study, we therefore restrict our analysis to GRBs that are less than ~ 70 degrees off axis, and conduct a study of the median, the lowest and the highest background fluence values. For these GRBs, the lower background count rates reflect a drop in the effective area for LLE events, and *should therefore not be interpreted as GRBs with necessarily lower gamma-ray backgrounds*. Finally, as long GRBs are expected to be uniformly distributed across the sky [74], we may assume a representative ALP-photon conversion probability $P_{a\gamma}$, shown in Fig. 3, for each considered background in our analysis (albeit, the GRB distribution may be anisotropic if the unassociated sources are very close-by.)

B. Simulating the ALP spectrum

To simulate ALP-induced gamma-ray spectra, we use the `xSPEC`'s `fakeit` function. We consider the ALP spectra in the energy range given by the LLE data file specifications, starting at ~ 30 MeV and reaching the GeV energies. We use the response function and the background observation derived previously from each considered LLE-detected GRB. On top of the scaled ALP-induced gamma-ray signal from Fig. 2, we add a realization of the background, taken to be a power-law approximation to the channels' photon rate fits for each considered GRB. The combination of the signal and the background is then passed through the `xSPEC`'s `fakeit` function to create 2000 realizations of spectra corresponding to different normalization values of

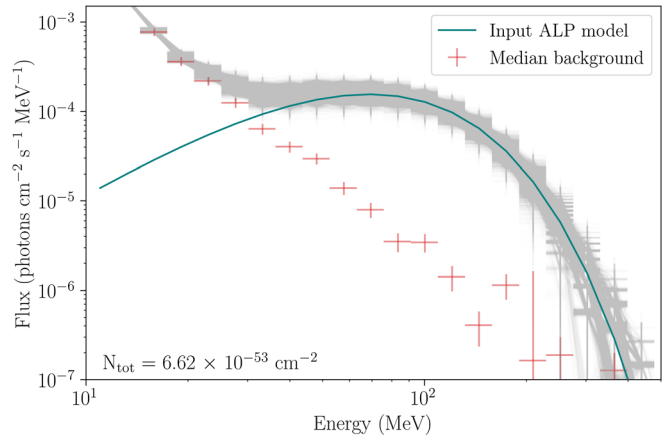


FIG. 5. `xSPEC` `fakeit` ALP simulations [75]. Shown in gray is a sample of 2000 realizations of the ALP spectrum for a $10-M_{\odot}$ progenitor and normalization $N_{\text{tot}} = 6.62 \times 10^{-53} \text{ cm}^{-2}$ (corresponding to a ~ 1 -Mpc distant CCSN with $P_{a\gamma} = 0.1$ and $g_{a\gamma} = 5.3 \times 10^{-12} \text{ GeV}^{-1}$ [47]) on top of the median background, including the background statistical and systematic uncertainties produced with `gburst`. The solid blue line represents the input ALP signal for the quoted normalization value.

the ALP signal on top of the observed background levels. An example of a simulation sample resulting from the `xSPEC`'s `fakeit` function is shown in Fig. 5.

C. Sensitivity results

To find the *Fermi*-LAT sensitivity to detecting ALP-induced gamma-ray signal originating from a given CCSN using the LLE data, we consider the highest, the lowest, and the median background levels as seen in our GRB sample, respectively corresponding to backgrounds of GRB 081024B, GRB 100826A, and GRB 121011A (also corresponding to the low, high, and medium θ s; see Fig. 4). We consider a grid of normalization values for the ALP spectrum, N_{tot} , between $8.4 \times 10^{-60} \text{ cm}^{-2}$ and $8.4 \times 10^{-50} \text{ cm}^{-2}$, motivated by *Fermi*-LATs expected flux sensitivity. For each of the three background levels, we add the normalized ALP spectrum (60 steps within the range quoted above) and produce 2000 simulations for each data realization for two different progenitor masses (10- and $18-M_{\odot}$), resulting in a total of 720,000 simulated spectra. Finally, we conduct spectral fitting for each spectrum, considering two different spectral models. The first model is the ALP model described in Sec. II with one free parameter, the total normalization N_{tot} , on top of the background model described by a power law with the normalization and power-index as free parameters. The second model is the background-only fit. For both cases, we use `xSPEC`'s `pgstat` statistical method, which describes Poisson data with Gaussian background [87]. Finally, we utilize Wilks' theorem as applied to the scenario in which the ALP signal, given a large

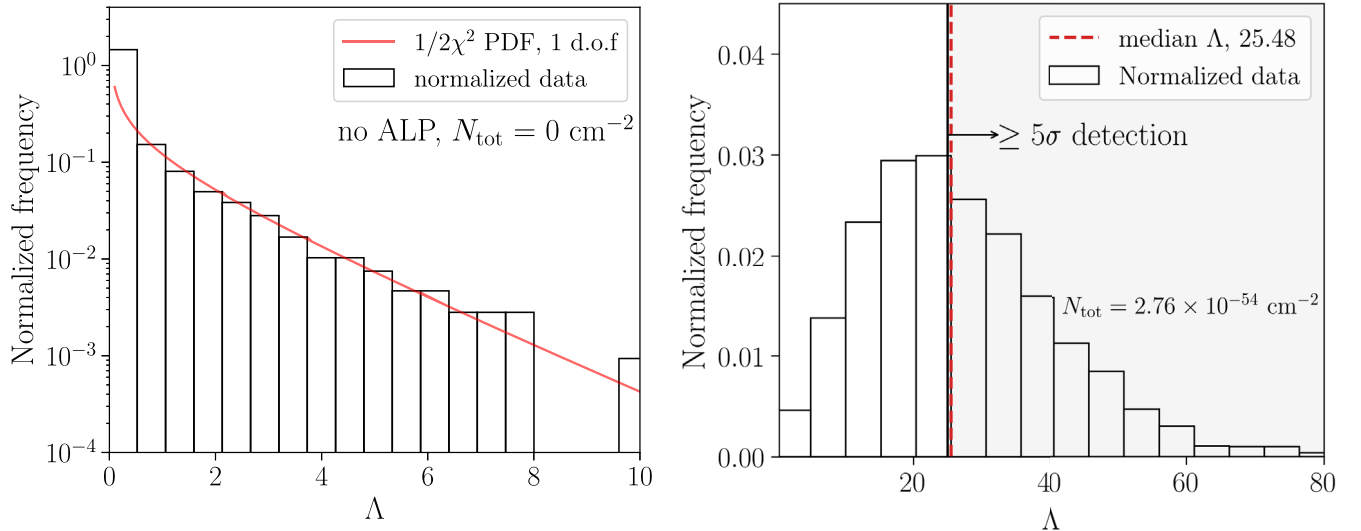


FIG. 6. Left: demonstration of Wilks’ theorem for the considered simulated spectra [88,89]. The red line is the half- χ^2 distribution with 1 d.o.f. on top of our normalized Λ distribution when no additional ALP signal is injected to the median background. Right: the distribution of the same $\Lambda = -2 \log(L_{\text{null}}/L_{\text{alternative}})$ when an additional ALP signal is injected to the median background. The null model remains the one without an additional ALP component, but the realizations are now drawn from a model with $N_{\text{tot}} = 2.76 \times 10^{-54} \text{ cm}^{-2}$, for the case of the median background and a progenitor mass of $10 M_{\odot}$. The median Λ represents the median value of the histogram. We determine the sensitivity of our experiment to a deviation from a no-ALP scenario, corresponding to a threshold of 5σ or the p -value of 5.7×10^{-7} .

number of realizations of data, the test statistic $\Lambda = -2 \log(L_{\text{null}}/L_{\text{alternative}})$, follows a half- χ^2 distribution [88,89], when no additional ALP signal is injected. In our case, L_{null} is the background-only fit, $L_{\text{alternative}}$ is the ALP model fit, and the difference in the number of degrees of freedom (d.o.f.) is 1 (ALP normalization). For each background consideration, we find a critical signal normalization for which we claim that the ALP model is preferred—taken to be when the log-likelihood analysis indicates half of the Λ values that would have probabilities less than 5.7×10^{-7} if the background-only hypothesis was correct, corresponding to a 5σ detection. We use 60 grid steps within the N_{tot} normalization range quoted above, with 30 of them a refinement, to accurately determine this “turn-over” point. An example of Λ distributions for a $10 M_{\odot}$ progenitor for the median background (GRB 121011A) is shown in Fig. 6.

The values of Λ corresponding to normalization values of $N_{\text{tot}} = 3.46 \times 10^{-54} \text{ cm}^{-2}$ for GRB 100826A (lowest background, high θ), $N_{\text{tot}} = 2.76 \times 10^{-54} \text{ cm}^{-2}$ for GRB 121011A (median background, medium θ), and $N_{\text{tot}} = 1.51 \times 10^{-54} \text{ cm}^{-2}$ for GRB081024A (highest background, low θ), for a $10 M_{\odot}$ progenitor, favor the ALP model over the background-only model. For a given ALP coupling g_{ay} , Fig. 7 shows the maximum allowed distance to a CCSNe for which a $5\text{-}\sigma$ ALP signal discovery can be expected (provided the given gamma-ray background and P_{ay} assumed from Fig. 3). On the other hand, if a time- and distance-tagged CCSN is observed without any detected ALP signal, then the yellow curve gives, on average, the expected 90% C.L.

upper limit to be derived on the ALP coupling g_{ay} . The right panel of Fig. 7 shows an analogous analysis, using the $18 M_{\odot}$ progenitor. For the lowest background (high θ), the corresponding normalization value is $N_{\text{tot}} = 1.56 \times 10^{-54} \text{ cm}^{-2}$; for the median background (medium θ) it is $N_{\text{tot}} = 1.30 \times 10^{-54} \text{ cm}^{-2}$; and finally, for the highest background (low θ) it is $N_{\text{tot}} = 7.06 \times 10^{-55} \text{ cm}^{-2}$. The corresponding distance limits for the deduced upper bound on coupling from the SN1987A analysis, $g_{\text{ay}} = 5.3 \times 10^{-12} \text{ GeV}^{-1}$ [47], in addition to a consideration of different conversion probabilities, are summarized in Table III. We remark that at the detection limit, only a few ALP-induced gamma-ray photons would be detected (~ 10 counts in the LLE sample), which makes it challenging to reliably reconstruct the energy spectrum or to alone trigger a GRB signal detection (considering the look-elsewhere effect in full sky surveys). Finally, we conclude the sensitivity analysis by noting that the distance limit variations in Fig. 7 are driven by differences in LLE effective area—thus, the lower background count rates, shown in Fig. 4, are mainly a consequence of decreasing detector acceptances at higher θ s.

V. SEARCH FOR AN ALP SIGNAL WITHIN THE SELECTED GRB SAMPLE

We consider the selected sample of unassociated GRBs in Table II and conduct a spectral fitting for each GRB to find the highest significance for an inclusion of the ALP spectral component. Although it is unlikely that a nearby

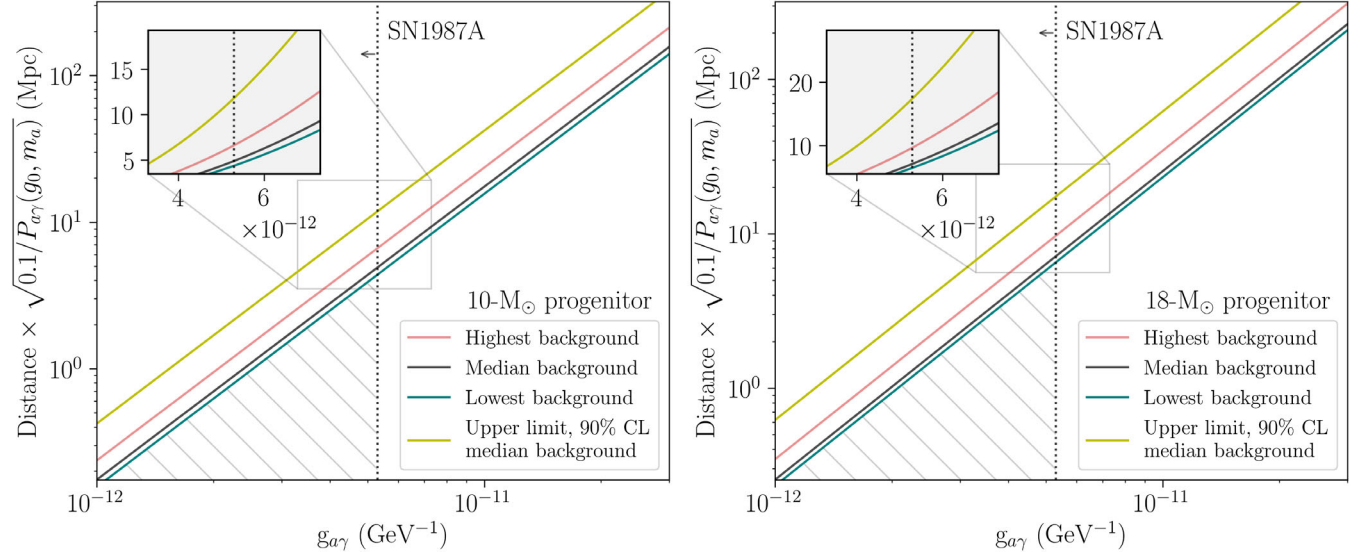


FIG. 7. Distance limits for a LAT-LLE ALP detection for a $10\text{-}M_{\odot}$ progenitor (left panel), and an $18\text{-}M_{\odot}$ progenitor (right). The green, black, and red solid lines represent the $5\text{-}\sigma$ detection limits on distances with so-far observed background levels from our GRB sample with *Fermi* LLE, while the yellow solid line represents the expected 90% C.L. upper limit for the median background. The dotted vertical line in each plot shows the upper limit for the ALP-photon coupling, $g_{a\gamma} = 5.3 \times 10^{-12} \text{ GeV}^{-1}$, derived in [47]. The hatching in both plots shows the parameter space to which *Fermi* LLE is sensitive, taking into consideration the SN1987A upper limit on the ALP-photon coupling.

star’s core collapse would remain an undetected CCSN to the current optical all-sky surveys, such as [90–95], or that an ordinary GRB would arrive without a time delay to the ALP signal from the core collapse, we here make the ansatz to search for an ALP signal only within the detected GRB signal time window. We consider a null model to include components commonly used to describe ordinary GRB emission, and compare it to the alternative including the additional ALP component.

TABLE III. Maximum distance to the ALP source to be within reach of the *Fermi*-LLE sensitivity. We assume the ALP-photon coupling $g_{a\gamma} = 5.3 \times 10^{-12} \text{ GeV}^{-1}$ [47] for different ALP-photon conversion probabilities, $P_{a\gamma}$, as seen in Fig. 3. Distance limits are in Mpc, shown for a $10\text{-}M_{\odot}$ progenitor on the left, and $18\text{-}M_{\odot}$ in parentheses on the right, for different background levels. Note that the different background levels are dependent on the LLE effective area, which decreases with an increase in θ , hence lowering the event rate in the detector (see Fig. 4). This, however, is not an indicator of the intrinsic GRB background levels, but rather detected counts in the instrument.

Conversion probability	Distance limit (Mpc)		
	Background level:		
$P_{\gamma}(g_0)$	Low	Median	High
0.1	4.4 (6.5)	4.9 (7.1)	6.6 (9.7)
0.05	3.1 (4.6)	3.5 (5.0)	4.7 (6.9)
0.01	1.4 (2.1)	1.5 (2.3)	2.1 (3.1)
0.001	0.4 (0.7)	0.5 (0.7)	0.7 (1.0)

A. Data preparation

The data in our sample was obtained from the public *Fermi Science Support Center* website [96]. To analyze data, we use the *Fermi Science Tools* [97] in combination with the HEASoft XSPEC spectral fitting software [98]. We conduct a combined analysis between GBM, LLE, and standard LAT transient data using the analysis tools commonly used in the high-energy transient community [75].

The GBM analysis is done using *gtburst* [99]. We conduct a binned analysis of the GBM data. First, we compute the overall signal-to-noise ratio for twelve GBM detectors and consider the three strongest signals recorded in the NaI detectors and one signal from a BGO detector for the spectral analysis. To determine the background, we use *gtburst* to specify off-signal intervals, fit a polynomial to each channel of the detector, and interpolate these polynomials to compute a background spectrum over a given time interval. For each GBM detector, we consider the same time interval of the burst, determined by visual inspection, approximately corresponding to the flattening of the light curve with the background level. The corresponding GRB duration is listed as T_{95} in Table II, reflecting the time interval reported in Table III in [74]. Finally, we produce spectral and background files appropriate for the analysis in XSPEC.

The preparation of the LLE data follows the same pathway as that of the GBM data. We assume the same burst duration as determined by the GBM value of T_{95} in Table II.

With its lower number of counts, LAT transient data requires a different approach utilizing an unbinned analysis. Due to the transient nature of the source, we make use of the event class `P8R3_TRANSIENT020_v2`, analyzed with the corresponding galactic and isotropic diffuse templates [100], over a time interval determined by the T_{95} values referenced in Table II. Using *gtburst*, for most GRBs, we perform a zenith cut of 100° , with a few-degree variation depending on a given source. We conduct a maximum likelihood analysis of the LAT source to obtain a LAT counts map within the considered region of interest (usually 12°). Once we obtain likelihood fit result parameters using *gtlike*, we proceed onto creating energy-binned background files using *gtbkg* and spectral files of energy-binned signal counts using *gtbin*, both readable by *XSPEC*. Throughout this analysis, we use the point-source localization information provided in the *Fermi* LAT Second GRB Catalog, 2FLGC [74].

B. XSPEC analysis

We conduct a standard spectral fitting procedure of the selected GRB sample [101]. Fitting is conducted in *PYXSPEC*, an object-oriented Python interface to *XSPEC* [102]. When modeling the spectral shape of a given GRB, we consider models commonly used in GRB spectral fitting, including single power law (denoted `pow` in Table II), power law with a high-energy exponential cutoff (also known as ‘‘comptonized model,’’ `cutoffpl`), the phenomenological Band function [86] (`grbm`), or a combination thereof. We also include a consideration of an additional thermal component in the form of a blackbody spectrum (`bb`), as suggested in [101,103]. Appendix provides the details about the used models. We apply *XSPEC*’s `pgstat` statistical method [87] and find the fit with the lowest test statistic (in *XSPEC* denoted by `PG-statistic`), obtaining profile log-likelihood (LL) values from the combined GBM, LLE and LAT transient data. We note that the ALP spectral model may be well reproduced for a specific range of parameters of the Band function; in particular, for a $10-M_\odot$ progenitor in Fig. 2 the corresponding Band model parameters are $\alpha_1 \simeq 2.4$, $\alpha_2 \simeq -0.1$, and $E_c \simeq 30$ MeV. However, in the considered GRB sample, these parameter values are not reached, as shown in Table II, and are not expected for ordinary GRB spectral shapes. Similarly, the ALP spectral shape can be reproduced reasonably well with a blackbody function described by a peak temperature of ~ 70 MeV; however, all the GRBs listed in Table II that are best fit by including a blackbody spectral component (GRBs 100826A, 110721A, 140102A, and 160917A) peak at the keV temperatures. For each model, we step through the neighboring fit parameter values to ensure that the best-fit parameters found from the maximum LL analysis are likely global, and not local minima.

To compare two nested models, we apply the log-likelihood ratio (LLR) test $\Lambda = -2 \log(L_{\text{GRB}}/L_{\text{GRB+ALP}})$, with

L_{GRB} corresponding to the likelihood of the null hypothesis, i.e., the GRB model constituting commonly used functions for ordinary GRB emission. $L_{\text{GRB+ALP}}$ corresponds to the alternative hypothesis, constituting an ALP signal added on top of the null model, with all the considered parameters left free to vary. Table II contains results of the model comparison of our data sample, using the $10-M_\odot$ -progenitor ALP spectral model. We note that the $18-M_\odot$ -progenitor has an almost identical spectral shape, leaving the results essentially independent on these two progenitor masses.

C. ALPs from GRBs: Fitting results

None of the GRBs in the considered sample showed a significant improvement in the fit when including the additional ALP signal component. The model comparison for one GRB, 101123A, indicates a Λ value of 5.8, corresponding to $\sim 2.4\sigma$ detection, pretrials. The data and the fitted models for GRB 101123A are shown in Fig. 8

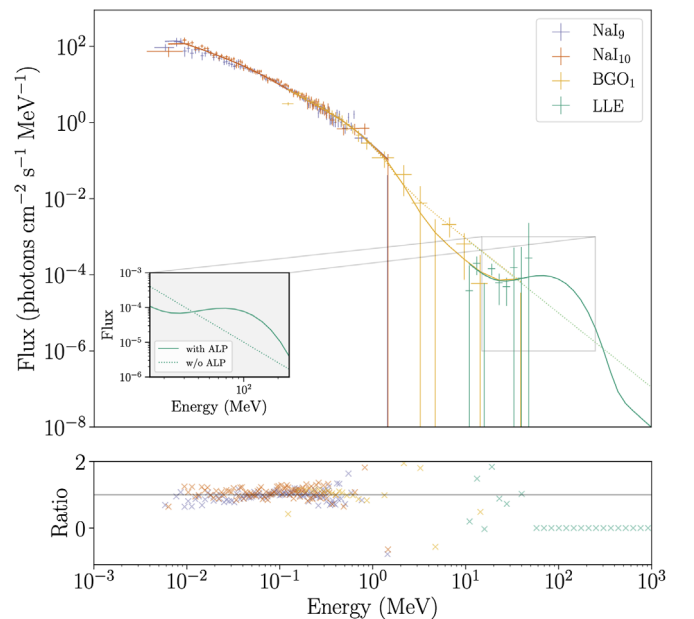


FIG. 8. GRB 101123A γ -ray flux with two different overlaid models. Different colors represent counts obtained by different detectors: purple, red, yellow, and blue correspond to NaI_9 , NaI_{10} , and BGO_1 detectors on GBM respectively; and green corresponds to the LLE transient data. The solid lines represent unfolded model fits for each instrument when the additional ALP component is included, whereas the dotted lines are the best-fit model without the additional ALP component. The inset shows the difference between the alternative and the null model in more detail: the solid green line represents the alternative model and the dotted line is the null model. The alternative model is composed of a Band function, exponential cutoff function, and the ALP signal. Finally, the lower panel shows the ratio of the observed data to the corresponding model that includes the ALP component, i.e., data/model. For plotting purposes only, the GBM data is shown binned, whilst LLE data is shown with the original binning provided by the instrument.

with an inplot showing the difference between the best null model and the alternative model with the additional ALP component.

This alternative best-fit hypothesis has an ALP component with the normalization $N_{\text{tot}} = 4.9 \times 10^{-52} \text{ cm}^{-2}$. Applying the coupling $g_{a\gamma} = 5.3 \times 10^{-12} \text{ GeV}^{-1}$ and a conversion probability $P_{a\gamma} = 0.01$ (see Fig. 3 for this GRB's sky position), we find that the corresponding distance would be ~ 120 kpc. Note that GRB 101123A was observed strongly off axis, at an incidence angle of $\sim 80^\circ$. Under such conditions, LLE's effective area decreases significantly. Thus, even a source with such a large N_{tot} value of the ALP component results in only few counts and no reconstructed energies above ~ 50 MeV.

We then include the trials factor [104], to take into account the size of the considered parameter space, and express the global significance by $p_{\text{global}} = 1 - (1 - p_{\text{local}})^{N_{\text{trials}}}$. From the local p -value, $p_{\text{local}} = 1.6 \times 10^{-4}$ and the number of GRB trials in our sample, $N_{\text{trials}} = 24$, this results in a global p -value of ~ 0.3 , further indicating that this observation is not statistically significant.

VI. CONCLUSIONS AND DISCUSSION

In this paper, we consider the light ALPs produced via the Primakoff process in a collapse of a massive star which, by converting into photons in the Galactic magnetic field, could produce an observable gamma-ray flux. The duration of an ALP burst is expected to be on the order of ~ 10 seconds. Due to its uncertain and likely negligible effect, we do not take into consideration the ALP-photon conversion that may take place in the magnetic field of the intergalactic medium and, due to a lack of magnetic field models, we do not take into consideration ALP-photon conversions that may take place within the host galaxy. In fact, the contribution from the host galaxy would increase the observed gamma-ray flux, rendering our current results conservative. Furthermore, due to the complexity of core-collapse modeling, we only consider two CCSN progenitor masses: $10 M_\odot$ and $18 M_\odot$ [47]. However, theoretical considerations suggest that long GRBs are produced in explosions of very massive ($\gtrsim 20 M_\odot$, [105]) stars which, in turn, would produce a higher number of ALPs as compared to a lower mass progenitor. Thus, the combination of our magnetic field and progenitor mass choices renders our reported results conservative.

We find the sensitivity of the *Fermi*-LAT instrument using the LLE data sample including energies $\gtrsim 30$ MeV to detect ALP-induced gamma-ray emission from CCSNe for ALP masses $m_a \lesssim 10^{-10}$ eV. In particular, we consider a sample of GRB backgrounds and compute the maximum allowed distance to core-collapsing stars that still give statistically significant, 5σ , ALP-signal detection. For the lowest background, we obtain that the limiting distance is ~ 3 Mpc for the conversion probability, $P_{a\gamma} = 0.05$, for a

$10 M_\odot$ progenitor, and ~ 5 Mpc for an $18 M_\odot$ progenitor, for a coupling of $g_{a\gamma} = 5.3 \times 10^{-12} \text{ GeV}^{-1}$ [47]. For the highest background count, the farthest distance corresponds to ~ 5 and ~ 7 Mpc; and for the median background, it is ~ 3.5 and ~ 5 Mpc for $10 M_\odot$ and $18 M_\odot$ progenitors respectively. Finally, the distance limits reported in this paper, in addition to the observed background levels, are driven by LLE effective area variation that tends to decrease for observations at larger instrumental incidence angles—and thus lower background count rates. These limiting distances for an ALP-signal detection from a CCSN for different conversion probabilities and axion-photon couplings $g_{a\gamma}$ are shown in Table III and Fig. 7. The results found in this paper by utilizing the LLE data cut technique and its resulting data sample are comparable to those done with the standard LAT analysis in [48]. As such, conducting a search for an ALP signal from a close-by CCSN using the LLE technique, independent from or in parallel with the standard LAT analysis, can be a useful way of probing the ALP parameter space. Furthermore, the distance limits found in this investigation may be complemented by utilizing the upper energy range of the better-resolved GBM data, or the rest of the LAT transient data, to search for the tail distribution from the ALP-induced gamma-ray emission.

Finally, we consider a sample of unassociated, thus potentially nearby, LLE-detected GRBs (see Table II). We conduct a spectral model fitting for each candidate using the XSPEC library models commonly used for GRB spectral modeling. Once the best fit for an ordinary GRB spectrum is determined, we conduct an analogous modeling procedure by introducing an additional ALP spectral component. We find that all of the GRB emissions in our sample are well fitted by commonly used GRB spectral models and that introducing an additional ALP spectral component does not result in a statistically significant improvement.

In this paper, we assume that the ALP-induced gamma-ray signal itself triggers the GRB observation or that the ALP signal from a CCSN coincides with the ordinary GRB signal, which is unlikely to be the case. The main source of uncertainty is determining the core-collapse time, and thus the expected arrival time of any ALP-induced GRB. Therefore, an interesting investigation would be a dedicated search for potential ALP induced gamma-ray photons arriving before the GRB trigger times. As suggested in [82], using optical light curves to predict explosion times may be another way of attempting these analyses, as done in [49]. Nevertheless, the optimal resolution for the time-tagging issue is using neutrino detection from a CCSN, followed by a search for ALP emission in the coincident gamma-ray observation; although, at this time, no such coincident detection has been confirmed in association with a GRB.

The GRB model comparison analysis does not allow for a deduction of the limits on the ALP coupling, $g_{a\gamma}$. In order

to obtain such information, we would require the GRBs' distance information, as done in [49]. With the current and upcoming optical surveys such as ASAS-SN [106], ZTF [107], TESS [108], and the Vera C. Rubin Observatory [109], the number of the observed nearby CCSNe (e.g. $z < 0.02$ or 100 Mpc), [49]) is likely to increase. This, in turn, would improve the probability of *Fermi* detecting their corresponding GRBs, allowing for a statistically significant study of such sources in the context of ALP searches and limits on the relevant ALP coupling space. An example of such an analysis determining the upper limits on the ALP coupling is shown in [49].

Furthermore, with the new generation of gamma-ray instruments, such as e-ASTROGAM [110], ComPair [111], PANGU [112], or the like, the improved sensitivity and angular resolution particularly at energies relevant to the ALP signal (< 100 MeV) and FoV's similar to *Fermi* LAT, the search for ALP-induced GRBs will be substantially improved. In particular, observatories such as AMEGO [113], with its excellent sensitivity, angular and energy resolution, low-energy threshold, and a large field of view, will allow for the most stringent constraints on the ALP parameter space, surpassing the limits of the current ALP laboratory experiments [114].

Finally, besides CCSNe, additional astrophysical objects may be considered as sites of ALP production. In particular, a production of ALPs has been hypothesized during neutron-star (NS) mergers; albeit further theoretical work is needed to constrain the expected ALP spectrum from such events [115]. Taking into consideration the most recent observations from NS mergers using e.g. LIGO/Virgo [116], as well as a rapid development of the field of gravitational wave astronomy, using gravitational waves may be yet another probe into the production time and nature of ALPs in the future.

ACKNOWLEDGMENTS

The authors thank Miguel A. Sánchez-Conde for discussion and detailed feedback. M.C. acknowledges support by NASA under Grant No. 80GSFC21M0002. M.M. acknowledges support from the European Research Council (ERC) under the European Union's Horizon 2020 research and innovation program Grant Agreement No. 948689 (AxionDM) and from the Deutsche Forschungsgemeinschaft (DFG, German Research Foundation) under Germany's Excellence Strategy—EXC 2121 “Quantum Universe”—390833306. The *Fermi* LAT collaboration acknowledges generous ongoing support from a number of agencies and institutes that have supported both the development and the operation of the LAT as well as scientific data analysis. These include the National Aeronautics and Space Administration and the Department of Energy in the United States, the

Commissariat à l'Energie Atomique and the Centre National de la Recherche Scientifique/Institut National de Physique Nucléaire et de Physique des Particules in France, the Agenzia Spaziale Italiana and the Istituto Nazionale di Fisica Nucleare in Italy, the Ministry of Education, Culture, Sports, Science and Technology (MEXT), High Energy Accelerator Research Organization (KEK) and Japan Aerospace Exploration Agency (JAXA) in Japan, and the K. A. Wallenberg Foundation, the Swedish Research Council and the Swedish National Space Board in Sweden. Additional support for science analysis during the operations phase is gratefully acknowledged from the Istituto Nazionale di Astrofisica in Italy and the Centre National d'Études Spatiales in France. This work was performed in part under DOE Contract No. DE-AC02-76SF00515.

APPENDIX: GRB Models

To fit the selected GRB sample, we use XSPEC models that include:

- (1) Band function (grbm, gamma-ray burst continuum), described by

$$A(E) = \begin{cases} KE^{\alpha_1} \exp(-E/E_c), & \text{if } E < E_c(\alpha_1 - \alpha_2) \\ K[(\alpha_1 - \alpha_2)E_c]^{(\alpha_1 - \alpha_2)} \exp(\alpha_2 - \alpha_1)E^{\alpha_2} & \\ \text{otherwise,} & \end{cases} \quad (\text{A1})$$

where E is the energy in units of keV. Model parameters are α_1 , first power-law index; α_2 , second power-law index; E_c , characteristic energy in keV; and K is the normalization constant in units of photons/keV/cm²/s.

- (2) Power law (pow) described by

$$A(E) = KE^{-\alpha}, \quad (\text{A2})$$

where α is the power-law index.

- (3) Power law with high energy exponential cutoff (cutoffpl) described by

$$A(E) = KE^{-\alpha} \exp(-E/\beta), \quad (\text{A3})$$

where β is the e -folding energy of the exponential rolloff (in keV).

- (iv) Blackbody spectrum (bb) described by

$$A(E) = K \frac{E^2}{\exp(E/kT) - 1}, \quad (\text{A4})$$

where kT is the temperature in keV.

- [1] J.E. Kim and G. Carosi, Axions and the strong CP problem, *Rev. Mod. Phys.* **82**, 557 (2010).
- [2] J. Jaeckel and A. Ringwald, The low-energy frontier of particle physics, *Annu. Rev. Nucl. Part. Sci.* **60**, 405 (2010).
- [3] A. Ringwald, Axions and axionlike particles, [arXiv:1407.0546](https://arxiv.org/abs/1407.0546).
- [4] D. J. Marsh, Axion cosmology, *Phys. Rep.* **643**, 1 (2016).
- [5] R. Peccei and H. Quinn, CP Conservation in the Presence of Pseudoparticles, *Phys. Rev. Lett.* **38**, 1440 (1977).
- [6] R. Peccei and H. Quinn, Constraints imposed by CP conservation in the presence of pseudoparticles, *Phys. Rev. D* **16**, 1791 (1977).
- [7] S. Weinberg, A New Light Boson?, *Phys. Rev. Lett.* **40**, 223 (1978).
- [8] F. Wilczek, Problem of Strong P and T Invariance in the Presence of Instantons, *Phys. Rev. Lett.* **40**, 279 (1978).
- [9] G. Raffelt and L. Stodolsky, Mixing of the photon with low mass particles, *Phys. Rev. D* **37**, 1237 (1988).
- [10] J.P. Conlon and M.C.D. Marsh, Excess Astrophysical Photons from a 0.1–1 keV Cosmic Axion Background, *Phys. Rev. Lett.* **111**, 151301 (2013).
- [11] S. Angus, J.P. Conlon, M.C.D. Marsh, A.J. Powell, and L.T. Witkowski, Soft x-ray excess in the coma cluster from a cosmic axion background, *J. Cosmol. Astropart. Phys.* **09** (2014) 026.
- [12] A.J. Powell, A cosmic ALP background and the cluster soft x-ray excess in A665, A2199 and A2255, *J. Cosmol. Astropart. Phys.* **09** (2015) 017.
- [13] D. Kraljic, M. Rummel, and J.P. Conlon, ALP conversion and the soft x-ray excess in the outskirts of the Coma cluster, *J. Cosmol. Astropart. Phys.* **01** (2015) 011.
- [14] M. Cicoli, J.P. Conlon, M.C.D. Marsh, and M. Rummel, 3.55 keV photon line and its morphology from a 3.55 keV axionlike particle line, *Phys. Rev. D* **90**, 023540 (2014).
- [15] A. Mirizzi and D. Montanino, Stochastic conversions of TeV photons into axionlike particles in extragalactic magnetic fields, *J. Cosmol. Astropart. Phys.* **12** (2009) 004.
- [16] M. Meyer, D. Horns, and M. Raue, First lower limits on the photon-axionlike particle coupling from very high energy gamma-ray observations, *Phys. Rev. D* **87**, 035027 (2013).
- [17] G. Galanti, M. Roncadelli, A. De Angelis, and G.F. Bignami, Hint at an axionlike particle from the redshift dependence of blazar spectra, *Mon. Not. R. Astron. Soc.* **493**, 1553 (2020).
- [18] K. Kohri and H. Kodama, Axionlike particles and recent observations of the cosmic infrared background radiation, *Phys. Rev. D* **96**, 051701 (2017).
- [19] J. Zhou, Z. Wang, F. Huang, and L. Chen, A possible blazar spectral irregularity case caused by photon-axionlike-particle oscillations, *J. Cosmol. Astropart. Phys.* **08** (2021) 007.
- [20] M. Giannotti, I. Irastorza, J. Redondo, and A. Ringwald, Cool WISPs for stellar cooling excesses, *J. Cosmol. Astropart. Phys.* **05** (2016) 057.
- [21] M. Giannotti, Hints of new physics from stars, *Proc. Sci. ICHEP2016* (2016) 076 [[arXiv:1611.04651](https://arxiv.org/abs/1611.04651)].
- [22] M. Giannotti, I. G. Irastorza, J. Redondo, A. Ringwald, and K. Saikawa, Stellar recipes for axion hunters, *J. Cosmol. Astropart. Phys.* **10** (2017) 010.
- [23] C. Dessert, A.J. Long, and B.R. Safdi, No evidence for axions from Chandra observation of magnetic white dwarf, [arXiv:2104.12772](https://arxiv.org/abs/2104.12772).
- [24] E. Aprile *et al.* (XENON Collaboration), Excess electronic recoil events in XENON1T, *Phys. Rev. D* **102**, 072004 (2020).
- [25] L. Di Luzio, M. Fedele, M. Giannotti, F. Mescia, and E. Nardi, Solar Axions Cannot Explain the XENON1T Excess, *Phys. Rev. Lett.* **125**, 131804 (2020).
- [26] C. Gao, J. Liu, L.-T. Wang, X.-P. Wang, W. Xue, and Y.-M. Zhong, Reexamining the Solar Axion Explanation for the XENON1T Excess, *Phys. Rev. Lett.* **125**, 131806 (2020).
- [27] K. Choi, S.H. Im, and C.S. Shin, Recent progress in physics of axions or axionlike particles, [arXiv:2012.05029](https://arxiv.org/abs/2012.05029).
- [28] P. Arias, D. Cadamuro, M. Goodsell, J. Jaeckel, J. Redondo, and A. Ringwald, WISPy cold dark matter, *J. Cosmol. Astropart. Phys.* **06** (2012) 013.
- [29] J. Preskill, M. B. Wise, and F. Wilczek, Cosmology of the invisible axion, *Phys. Lett.* **120B**, 127 (1983).
- [30] L. F. Abbott and P. Sikivie, A cosmological bound on the invisible axion, *Phys. Lett.* **120B**, 133 (1983).
- [31] M. Dine and W. Fischler, The not so harmless axion, *Phys. Lett.* **120B**, 137 (1983).
- [32] K. Ehret *et al.*, New ALPs results on hidden-sector lightweights, *Phys. Lett. B* **689**, 149 (2010).
- [33] L. D. Duffy, P. Sikivie, D. B. Tanner, S. J. Asztalos, C. Hagmann, D. Kinion, L. J. Rosenberg, K. van Bibber, D. B. Yu, and R. F. Bradley (ADMX Collaboration), A high resolution search for dark-matter axions, *Phys. Rev. D* **74**, 012006 (2006).
- [34] A. Friedland, M. Giannotti, and M. Wise, Constraining the Axion-Photon Coupling with Massive Stars, *Phys. Rev. Lett.* **110**, 061101 (2013).
- [35] A. Ayala, I. Domnguez, M. Giannotti, A. Mirizzi, and O. Straniero, Revisiting the Bound on Axion-Photon Coupling from Globular Clusters, *Phys. Rev. Lett.* **113**, 191302 (2014).
- [36] C. Dessert, J. W. Foster, and B. R. Safdi, X-ray Searches for Axions from Super Star Clusters, *Phys. Rev. Lett.* **125**, 261102 (2020).
- [37] M. Ajello *et al.* (Fermi-LAT Collaboration), Search for Spectral Irregularities due to Photon–Axionlike-Particle Oscillations with the Fermi Large Area Telescope, *Phys. Rev. Lett.* **116**, 161101 (2016).
- [38] J.-G. Cheng, Y.-J. He, Y.-F. Liang, R.-J. Lu, and E.-W. Liang, Revisiting the analysis of axionlike particles with the Fermi-LAT gamma-ray observation of NGC1275, *Phys. Lett. B* **821**, 136611 (2021).
- [39] M. D. Marsh, H. R. Russell, A. C. Fabian, B. R. McNamara, P. Nulsen, and C. S. Reynolds, A new bound on axionlike particles, *J. Cosmol. Astropart. Phys.* **12** (2017) 036.
- [40] D. Malyshev, A. Neronov, D. Semikoz, A. Santangelo, and J. Jochum, Improved limit on axionlike particles from γ -ray data on Perseus cluster, [arXiv:1805.04388](https://arxiv.org/abs/1805.04388).

- [41] C. S. Reynolds, M. C. D. Marsh, H. R. Russell, A. C. Fabian, R. Smith, F. Tombesi, and S. Veilleux, Astrophysical limits on very light axionlike particles from Chandra grating spectroscopy of NGC 1275, [arXiv:1907.05475](https://arxiv.org/abs/1907.05475).
- [42] H. Primakoff, Photoproduction of neutral mesons in nuclear electric fields and the mean life of the neutral meson, *Phys. Rev.* **81**, 899 (1951).
- [43] T. Fischer, S. C. Whitehouse, A. Mezzacappa, F. K. Thielemann, and M. Liebendorfer, Protoneutron star evolution and the neutrino driven wind in general relativistic neutrino radiation hydrodynamics simulations, *Astron. Astrophys.* **517**, A80 (2010).
- [44] G. G. Raffelt, Astrophysical axion bounds diminished by screening effects, *Phys. Rev. D* **33**, 897 (1986).
- [45] J. Brockway, E. Carlson, and G. Raffelt, SN 1987A gamma-ray limits on the conversion of pseudoscalars, *Phys. Lett. B* **383**, 439 (1996).
- [46] J. A. Grifols, E. Massó, and R. Toldrà, Gamma rays from SN 1987A due to pseudoscalar conversion, *Phys. Rev. D* **77**, 2372 (1996).
- [47] A. Payez, C. Evoli, T. Fischer, M. Giannotti, A. Mirizzi, and A. Ringwald, Revisiting the SN1987A gamma-ray limit on ultralight axionlike particles, *J. Cosmol. Astropart. Phys.* **02** (2015) 006.
- [48] M. Meyer, M. Giannotti, A. Mirizzi, J. Conrad, and M. A. Sánchez-Conde, Fermi Large Area Telescope as a Galactic Supernovae Axionscope, *Phys. Rev. Lett.* **118**, 011103 (2017).
- [49] M. Meyer and T. Petrushevska, Search for Axionlike-Particle-Induced Prompt γ -Ray Emission from Extragalactic Core-Collapse Supernovae with the *Fermi* Large Area Telescope, *Phys. Rev. Lett.* **124**, 231101 (2020); Erratum, *Phys. Rev. Lett.* **125**, 119901 (2020).
- [50] T. Piran, The physics of gamma-ray bursts, *Rev. Mod. Phys.* **76**, 1143 (2005).
- [51] J. P. Norris, T. L. Cline, U. D. Desai, and B. J. Teegarden, Frequency of fast, narrow gamma-ray bursts, *Nature (London)* **308**, 434 (1984).
- [52] C. Kouveliotou, C. A. Meegan, G. J. Fishman, N. P. Bhat, M. S. Briggs, T. M. Koshut, W. S. Paciesas, and G. N. Pendleton, Identification of two classes of gamma-ray bursts, *Astrophys. J. Lett.* **413**, L101 (1993).
- [53] E. Berger, Short-duration gamma-ray bursts, *Annu. Rev. Astron. Astrophys.* **52**, 43 (2014).
- [54] W. Fong and E. Berger, The locations of short gamma-ray bursts as evidence for compact object binary progenitors, *Astrophys. J.* **776**, 18 (2013).
- [55] W. Fong, E. Berger, R. Margutti, and B. A. Zauderer, A decade of short-duration gamma-ray burst broadband afterglows: Energetics, circumburst densities, and jet opening angles, [arXiv:1509.02922](https://arxiv.org/abs/1509.02922).
- [56] B. P. Abbott *et al.* (LIGO Scientific, Virgo, Fermi-GBM, INTEGRAL Collaborations), Gravitational waves and gamma rays from a binary neutron star merger: GW170817 and GRB 170817A, *Astrophys. J.* **848**, L13 (2017).
- [57] T. J. Galama *et al.*, An unusual supernova in the error box of the γ -ray burst of 25 April 1998, *Nature (London)* **395**, 670 (1998).
- [58] F. Patat *et al.*, The metamorphosis of SN1998bw, *Astrophys. J.* **555**, 900 (2001).
- [59] S. E. Woosley and J. S. Bloom, The supernova gamma-ray burst connection, *Annu. Rev. Astron. Astrophys.* **44**, 507 (2006).
- [60] E. Bissaldi, F. Calura, F. Matteucci, F. Longo, and G. Barbiellini, The connection between gamma-ray bursts and supernovae Ib/c, *Astron. Astrophys.* **471**, 585 (2007).
- [61] M. Della Valle, Supernovae and gamma-ray bursts: A decade of observations, *Int. J. Mod. Phys. D* **20**, 1745 (2011).
- [62] Z. Cano, S.-Q. Wang, Z.-G. Dai, and X.-F. Wu, The observers guide to the gamma-ray burst supernova connection, *Adv. Astron.* **2017**, 1 (2017).
- [63] C. Meegan *et al.*, The fermi gamma-ray burst monitor, *Astrophys. J.* **702**, 791 (2009).
- [64] W. B. Atwood, A. A. Abdo, M. Ackermann, W. Althouse, B. Anderson, M. Axelsson, L. Baldini, J. Ballet, D. L. Band, G. Barbiellini *et al.*, The large area telescope on the fermi gamma-ray space telescope mission, *Astrophys. J.* **697**, 1071 (2009).
- [65] V. Pelassa, R. Preece, F. Piron, N. Omodei, and S. Guiriec, The LAT low-energy technique for Fermi gamma-ray bursts spectral analysis, [arXiv:1002.2617](https://arxiv.org/abs/1002.2617).
- [66] A. Dobrynina, A. Kartavtsev, and G. Raffelt, Photon-photon dispersion of TeV gamma rays and its role for photon-ALP conversion, *Phys. Rev. D* **91**, 083003 (2015); Erratum, *Phys. Rev. D* **95**, 109905 (2017).
- [67] R. Buehler, G. Gallardo, G. Maier, A. Domínguez, M. López, and M. Meyer, Search for the imprint of axionlike particles in the highest-energy photons of hard γ -ray blazars, *J. Cosmol. Astropart. Phys.* **09** (2020) 027.
- [68] M. Libanov and S. Troitsky, On the impact of magnetic-field models in galaxy clusters on constraints on axionlike particles from the lack of irregularities in high-energy spectra of astrophysical sources, [arXiv:1908.03084](https://arxiv.org/abs/1908.03084).
- [69] M. A. Buen-Abad, J. Fan, and C. Sun, Constraints on axions from cosmic distance measurements, [arXiv:2011.05993](https://arxiv.org/abs/2011.05993).
- [70] R. Jansson and G. Farrar, A new model of the galactic magnetic field, *Astrophys. J.* **757**, 14 (2012).
- [71] M. Meyer, GammaALPs: Calculating the conversion probability between photons and axions/axionlike particles in various astrophysical magnetic fields, <https://github.com/me-manu/gammaALPs> (2021).
- [72] M. Meyer, D. Horns, and M. Raue, First lower limits on the photon-axionlike particle coupling from very high energy gamma-ray observations, *Phys. Rev. D* **87**, 035027 (2013).
- [73] P. Carena, C. Evoli, M. Giannotti, A. Mirizzi, and D. Montanino, Turbulent axion-photon conversions in the Milky Way, *Phys. Rev. D* **104**, 023003 (2021).
- [74] M. Ajello *et al.*, A Decade of gamma-ray bursts observed by Fermi-LAT: The second GRB catalog, *Astrophys. J.* **878**, 52 (2019).
- [75] K. Arnaud, B. Dorman, and C. Gordon, XSPEC: An x-ray spectral fitting package (1999), [ascl:9910.005](https://www.ascl.net/9910.005), <https://www.ascl.net/9910.005>; K. A. Arnaud, XSPEC: The First Ten Years, <https://ui.adsabs.harvard.edu/abs/1996ASPC..101...17A/abstract>.
- [76] <https://heasarc.gsfc.nasa.gov/docs/xanadu/xspec/python/html/index.html> (2019).

- [77] M. Ajello *et al.* (Fermi-LAT Collaboration), Impulsive and long duration high-energy gamma-ray emission from the very bright 2012 March 7 solar flares, *Astrophys. J.* **789**, 20 (2014).
- [78] <https://heasarc.gsfc.nasa.gov/W3Browse/fermi/fermille.html> (2019).
- [79] IceCube Collaboration, Neutrino emission from the direction of the blazar TXS 0506 + 056 prior to the IceCube-170922A alert, *Science* **361**, 147 (2018).
- [80] S. Ando, J. F. Beacom, and H. Yuksel, Detection of Neutrinos from Supernovae in Nearby Galaxies, *Phys. Rev. Lett.* **95**, 171101 (2005).
- [81] M. D. Kistler, H. Yuksel, S. Ando, J. F. Beacom, and Y. Suzuki, Core-collapse astrophysics with a five-megaton neutrino detector, *Phys. Rev. D* **83**, 123008 (2011).
- [82] D. F. Cowen, A. Franckowiak, and M. Kowalski, Estimating the explosion time of core-collapse supernovae from their optical light curves, *Astropart. Phys.* **33**, 19 (2010).
- [83] S. E. Woosley, Models for gamma-ray burst progenitors and central engines, [arXiv:1105.4193](https://arxiv.org/abs/1105.4193).
- [84] Y. F. Huang, Z. G. Dai, and T. Lu, Failed gamma-ray bursts and orphan afterglows, *Mon. Not. R. Astron. Soc.* **332**, 735 (2002).
- [85] <https://heasarc.gsfc.nasa.gov/W3Browse/fermi/fermilgrb.html>.
- [86] D. Band, J. Matteson, L. Ford, B. Schaefer, D. Palmer, B. Teegarden, T. Cline, M. Briggs, W. Paciesas, G. Pendleton, G. Fishman, C. Kouveliotou, C. Meegan, R. Wilson, and P. Lestrade, BATSE observations of gamma-ray burst spectra. I. Spectral diversity, *Astrophys. J.* **413**, 281 (1993).
- [87] G. Vianello, The significance of an excess in a counting experiment: Assessing the impact of systematic uncertainties and the case with a Gaussian background, *Astrophys. J. Suppl. Ser.* **236**, 17 (2018).
- [88] S. S. Wilks, The large-sample distribution of the likelihood ratio for testing composite hypotheses, *Ann. Math. Stat.* **9**, 60 (1938).
- [89] G. Cowan, K. Cranmer, E. Gross, and O. Vitells, Asymptotic formulae for likelihood-based tests of new physics, *Eur. Phys. J. C* **71**, 1554 (2011); Erratum, *Eur. Phys. J. C* **73**, 2501 (2013).
- [90] G. Pojmanski, The All Sky Automated Survey. Variable stars in the 0h–6h quarter of the southern hemisphere, *Acta Astronaut.* **52**, 397 (2002), http://acta.astro.uw.edu/pl/Vol52/n4/a_52_4_4.html.
- [91] B. J. Shappee *et al.*, The man behind the curtain: X rays drive the UV through NIR variability in the 2013 AGN outburst in NGC 2617, *Astrophys. J.* **788**, 48 (2014).
- [92] J. L. Tonry, L. Denneau, A. N. Heinze, B. Stalder, K. W. Smith, S. J. Smartt, C. W. Stubbs, H. J. Weiland, and A. Rest, ATLAS: A high-cadence all-sky survey system, [arXiv:1802.00879](https://arxiv.org/abs/1802.00879).
- [93] P. R. Woniak, W. T. Vestrand, C. W. Akerlof, R. Balsano, J. Bloch, D. Casperon, S. Fletcher, G. Gisler, R. Kehoe, K. Kinemuchi *et al.*, Northern sky variability survey (NSVS): Public data release, *Astron. J.* **127**, 2436 (2004).
- [94] A. J. Drake, S. G. Djorgovski, A. Mahabal, E. Beshore, S. Larson, M. J. Graham, R. Williams, E. Christensen, M. Catelan, A. Boattini *et al.*, First results from the Catalina real-time transient survey (CRTS), *Astrophys. J.* **696**, 870 (2009).
- [95] N. M. Law, S. R. Kulkarni, R. G. Dekany, E. O. Ofek, R. M. Quimby, P. E. Nugent, J. Surace, C. C. Grillmair, J. S. Bloom, M. M. Kasliwal *et al.*, The palomar transient factory (PTF): System overview, performance, and first results, *Publ. Astron. Soc. Pac.* **121**, 1395 (2009).
- [96] <https://fermi.gsfc.nasa.gov/ssc/data/> (2019).
- [97] <https://fermi.gsfc.nasa.gov/ssc/data/analysis/software/> (2019).
- [98] <https://heasarc.gsfc.nasa.gov/lheasoft/> (2019).
- [99] <https://github.com/giacomov/gtburst>.
- [100] <https://fermi.gsfc.nasa.gov/ssc/data/access/lat/BackgroundModels.html> (2019).
- [101] B. B. Zhang, B. Zhang, E. Liang, Y. Fan, X. Wu, A. Pe’er, A. a. Maxham, H. Gao, and Y. Dong, A comprehensive analysis of fermi gamma-ray burst data. I. Spectral components and the possible physical origins of LAT/GBM GRBs, *Astrophys. J.* **730**, 141 (2011).
- [102] <https://heasarc.gsfc.nasa.gov/xanadu/xspec/python/html/index.html> (2019).
- [103] S. Guiriec *et al.*, Detection of a thermal spectral component in the prompt emission of GRB 100724B, *Astron. J.* **727**, L33 (2011).
- [104] L. Lyons, Open statistical issues in particle physics, *Ann. Appl. Stat.* **2**, 887 (2008).
- [105] A. Levan, Long-GRB progenitors, in *Gamma-Ray Bursts*, 2514-3433 (IOP Publishing, Bristol, UK, 2018), pp. 5–1 to 5–18.
- [106] T. W. Holoiien *et al.*, The ASAS-SN bright supernova catalogue—I. 2013–2014, *Mon. Not. R. Astron. Soc.* **464**, 2672 (2017).
- [107] E. C. Bellm *et al.*, The Zwicky transient facility: System overview, performance, and first results, *Publ. Astron. Soc. Pac.* **131**, 018002 (2019).
- [108] M. M. Fausnaugh *et al.*, Early time light curves of 18 bright type Ia supernovae observed with TESS, *Astrophys. J.* **908**, 51 (2021).
- [109] LSSTScience Collaboration, LSST Science Book, Version 2.0, [arXiv:0912.0201](https://arxiv.org/abs/0912.0201).
- [110] V. Tatischeff *et al.*, The e-ASTROGAM gamma-ray space mission, *Proc. SPIE Int. Soc. Opt. Eng.* **9905**, 99052N (2016).
- [111] A. Moiseev *et al.*, Compton-pair production space telescope (ComPair) for MeV gamma-ray astronomy, [arXiv:1508.07349](https://arxiv.org/abs/1508.07349).
- [112] X. Wu, M. Su, A. Bravar, J. Chang, Y. Fan, M. Pohl, and R. Walter, PANGU: A high resolution gamma-ray space telescope, *Proc. SPIE Int. Soc. Opt. Eng.* **9144**, 91440F (2014).
- [113] R. Caputo *et al.* (AMEGO Collaboration), All-sky medium energy gamma-ray observatory: Exploring the extreme multimessenger Universe, [arXiv:1907.07558](https://arxiv.org/abs/1907.07558).
- [114] https://www.snowmass21.org/docs/files/summaries/CF/SNOWMASS21-CF3_CF2_Regina_Caputo-122.pdf (2021).
- [115] S. P. Harris, J.-F. Fortin, K. Sinha, and M. G. Alford, Axions in neutron star mergers, *J. Cosmol. Astropart. Phys.* **07** (2020) 023.
- [116] LIGO Scientific Collaboration and Virgo Collaboration, GW170817: Observation of Gravitational Waves from a Binary Neutron Star Inspiral, *Phys. Rev. Lett.* **119**, 161101 (2017).